



# 2<sup>nd</sup> Advanced Optical Metrology Compendium

## Advanced Optical Metrology

Geoscience | Corrosion | Particles | Additive Manufacturing: Metallurgy, Cut Analysis & Porosity



**EVIDENT**  
**OLYMPUS**

**WILEY**

The latest eBook from **Advanced Optical Metrology**.  
Download for free.

This compendium includes a collection of optical metrology papers, a repository of teaching materials, and instructions on how to publish scientific achievements.

With the aim of improving communication between fundamental research and industrial applications in the field of optical metrology we have collected and organized existing information and made it more accessible and useful for researchers and practitioners.

**EVIDENT**  
**OLYMPUS**

**WILEY**

# Large-Area Low-Cost Multiscale-Hierarchical Metasurfaces for Multispectral Compatible Camouflage of Dual-Band Lasers, Infrared and Microwave

Xingdong Feng, Mingbo Pu,\* Fei Zhang, Rui Pan, Si Wang, Jintao Gong, Renyan Zhang, Yinghui Guo, Xiong Li, Xiaoliang Ma, and Xiangang Luo\*

Multispectral complementary detection technologies have made single-band camouflage materials ineffective, creating strong demand for multispectral compatible camouflage materials. Here, multiscale-hierarchical metasurfaces (MHM) compatible with large-area low-cost fabrication are proposed for the first time to realize multispectral camouflage of dual-band lasers, infrared and microwave. The MHM consists of an all-metallic metasurface array (AMMA) and a microwave absorber. The AMMA hinders dual-band lasers and thermal infrared detection, while the microwave absorber beneath the AMMA is applied as a defence against microwave detection. As a proof-of-concept, a MHM sample with an area of  $30 \times 30 \text{ cm}^2$  and a minimum linewidth of  $1.8 \text{ }\mu\text{m}$  is fabricated based on nanoimprint lithography. The excellent multispectral camouflage performance is verified in experiments, showing low reflectance ( $<0.2$ ) in  $0.9\text{--}1.2 \text{ }\mu\text{m}$  and  $9\text{--}12 \text{ }\mu\text{m}$ , low infrared emissivity ( $<0.2$ ), and high absorption efficiency of over 90%  $2.7\text{--}26 \text{ GHz}$ . Wide-angle and polarization-independent characteristics are also demonstrated. This work offers a promising opportunity for the engineering application of metasurfaces in the multispectral camouflage field. Moreover, this methodology can be easily extended to other electromagnetic spectrum, providing significant guidance for the design and fabrication of multispectral devices.

of camouflage technologies is promoted by fast-growing detection technologies. Multispectral complementary detection technologies, where detectors based on different principles and working bands can be used in combination, have made conventional single-band camouflage materials ineffective.<sup>[7,8]</sup> Thus, exploring multispectral compatible camouflage technologies becomes necessary. During the past decade, extensive studies have been performed to realize multispectral compatible camouflage.<sup>[8–12]</sup> However, research on laser-infrared-microwave compatible camouflage remains rare, because both the design and preparation of such compatible materials are very challenging.


Microwave radar, laser radar, and thermal infrared are three main detection technologies.<sup>[8,10,11]</sup> Microwave and laser radar, working on the active mode, distinguish the targets by analyzing the reflected radar signals.<sup>[13]</sup> Therefore, high absorption materials can be used to defend against microwave and laser detection by reducing the reflected wave from the targets.<sup>[14]</sup> In contrast, infrared cam-

ouflage materials generally expect low infrared emissivity,<sup>[15]</sup> which indicates low absorptance is required for infrared invisibility based on Kirchhoff's law.<sup>[16]</sup> To achieve multispectral compatible camouflage, materials are required to satisfy these conflicting parametric requirements simultaneously.

## 1. Introduction

The power of evolution by natural selection enables various animal camouflage strategies such as crypsis,<sup>[1,2]</sup> masquerade,<sup>[3]</sup> mimicry,<sup>[4]</sup> motion dazzle,<sup>[5]</sup> etc.<sup>[6]</sup> In human society, the evolution

X. Feng, M. Pu, F. Zhang, R. Pan, S. Wang, J. Gong, R. Zhang, Y. Guo, X. Li, X. Ma, X. Luo  
State Key Laboratory of Optical Technologies on Nano-Fabrication and Micro-Engineering  
Institute of Optics and Electronics  
Chinese Academy of Sciences  
Chengdu 610209, China  
E-mail: pmb@ioe.ac.cn; lxx@ioe.ac.cn

 The ORCID identification number(s) for the author(s) of this article can be found under <https://doi.org/10.1002/adfm.202205547>.

DOI: 10.1002/adfm.202205547

X. Feng, M. Pu, Y. Guo, X. Li, X. Ma, X. Luo  
School of Optoelectronics  
University of Chinese Academy of Sciences  
Beijing 100049, China  
R. Zhang  
Division of Frontier Science and Technology  
Institute of Optics and Electronics  
Chinese Academy of Sciences  
Chengdu 610209, China  
M. Pu, F. Zhang, Y. Guo  
Research center on vector optical fields  
Institute of Optics and Electronics  
Chinese Academy of Sciences  
Chengdu 610209, China

As a 2D version of metamaterials, metasurfaces can enable many novel phenomena and applications, such as catenary optics,<sup>[17–19]</sup> large field of view imaging,<sup>[20,21]</sup> multi-dimensions meta-holography,<sup>[22–24]</sup> asymmetric photonic spin-orbit interactions,<sup>[25,26]</sup> tunable multifunctional devices,<sup>[27,28]</sup> generalized Pancharatnam-Berry Phase,<sup>[29,30]</sup> and many others.<sup>[31–33]</sup> The ability of metasurfaces to arbitrarily control the light wavefronts provides a promising platform for multispectral camouflage technology.<sup>[34,35]</sup> Applying an infrared shielding layer with microwave-transparent property on a microwave absorber is a general way to realize microwave-infrared compatible camouflage.<sup>[10,36,37]</sup> Several metasurface absorbers have also been proposed to achieve laser-infrared compatible camouflage by designing a narrow working band around the laser wavelengths,<sup>[15,38]</sup> which, however, cannot cope with laser detectors with tunable frequency. As an alternative to electromagnetic absorption, virtual shaping can be used to conceal the targets from the radar detectors by controlling their electromagnetic shape.<sup>[35]</sup> Based on the above-mentioned principle, all-metallic metasurfaces have been presented to scatter the incoming energy in offset directions, leading to a null in specular direction and resulting in simultaneous laser-infrared or microwave-infrared invisibility.<sup>[11,39]</sup> The advantage of this laser-infrared camouflage strategy is to achieve broadband laser camouflage. Nevertheless, this reported laser-infrared material has a complicated structure and is fabricated based on the laser direct writing technique,<sup>[11]</sup> which are not suitable for large-area low-cost fabrication. In addition, to the best of our knowledge, there remains no report about experimental demonstrations of laser-infrared-microwave compatible camouflage via metasurfaces.

Besides metasurface-based structures, one-dimensional photonic crystals (1D-PCs) could also be used in multispectral camouflage.<sup>[8,15,40]</sup> Most recently, Zhu et al. developed multispectral camouflage for infrared, visible, lasers and microwave using 1D-PCs.<sup>[8]</sup> However, the fabrication of multilayer films (more than ten layers) is low-efficiency and high-cost, and the ultra-narrow working band for laser camouflage makes them ineffective against laser detectors with tunable frequency. Thereby, it is still difficult to design well-performed multispectral camouflage materials with: i) reduction of echo signals in various broadband ranges for defending against microwave and laser detectors; ii) low infrared emissivity for infrared concealment. Moreover, finding a suitable way to fabricate such multispectral camouflage materials with large-area and low-cost features is another significant issue.

In this paper, we propose and experimentally demonstrate multiscale-hierarchical metasurfaces (MHM) to achieve compatible camouflage of dual-band lasers, infrared and microwave. The MHM consists of an all-metallic metasurface array (AMMA) integrated with a microwave absorber. Two sizes of metallic cubes constitute the AMMA, which can effectively camouflage the targets against dual-band lasers without requiring complex structures; thus making it possible to accomplish its large-area low-cost fabrication via nanoimprint lithography (NIL). A broadband absorber with trilayered square patch metasurfaces is utilized to achieve microwave camouflage. As a proof-of-concept demonstration, a MHM sample with an area of  $30 \times 30 \text{ cm}^2$  and a minimum linewidth of  $1.8 \text{ }\mu\text{m}$  was fabricated and characterized, which exhibits excellent multispectral compatible

camouflage performance: i) reflectance in  $0.9\text{--}1.2 \text{ }\mu\text{m}$  and  $9\text{--}12 \text{ }\mu\text{m}$  are both less than 0.2; ii) low infrared emissivity ( $<0.2$ ) in the bands of  $3\text{--}5 \text{ }\mu\text{m}$  and  $8\text{--}14 \text{ }\mu\text{m}$ ; iii) high absorption efficiency of over 90% in the broadband of  $2.7\text{--}26 \text{ GHz}$ . Wide-angle and polarization-independent characteristics were also demonstrated. Together with the advantages such as good expansibility and ductility, high-productivity and low-cost fabrication, as well as lightweight, our design may promote the engineering applications of metasurfaces in the field of multispectral camouflage.

This paper is structured as follows. The design and simulations of the MHM are carried out in Section 2, which is followed by the fabrication and characterization of the proposed multispectral camouflage structure in Section 3. The conclusion of this work is included in Section 4, to finalize with more details on the simulation settings and experiments in Section 5.

## 2. Design and Simulations

In the beginning, we elaborate on our multispectral compatible camouflage strategy. A schematic of the proposed MHM is depicted in **Figure 1a**. At the top of the structures is an AMMA, which is composed of periodically arranged all-metallic metasurfaces. The all-metallic metasurface is built by two sizes of metallic cubes as shown in **Figure 1b**. The AMMA performs multiple roles here. First, for incoming electromagnetic waves in a dual-band involving the wavelengths of  $1.06$  and  $10.6 \text{ }\mu\text{m}$ , two significant working wavelengths of laser detectors in near-infrared (NIR) and long-wavelength infrared (LWIR), the AMMA can direct the reflected energy to non-specular angles to suppress the echo signal. Second, the AMMA can keep infrared emissivity low since there is no absorption. Third, it is also a microwave-transparent layer owing to the periodic arrangement of micrometer-scale slits in it. For the incoming microwave, after passing through the AMMA, high-efficiency absorption can be achieved by the microwave absorber at the bottom. The basic building bricks of the microwave absorber are composed of trilayered square patch metasurfaces with various sheet resistances, Polyethylene Terephthalate (PET) substrates, three intermediate spacers, and a back reflector that provides zero transmittance. In addition, due to the fourfold geometrical symmetry of the unit cells, our structures are almost insensitive to the polarization states of the incident waves.

Subsequently, we focus on the design of the dual-band lasers camouflage. In order to achieve echo signals reduction, applying absorption material on the surface and shaping the targets are two general ways.<sup>[41]</sup> For camouflage against  $10.6 \text{ }\mu\text{m}$  laser, absorption materials with ultra-narrow bandwidth are necessary because high absorptance conflicts with low emittance requirement in  $8\text{--}14 \text{ }\mu\text{m}$  for infrared invisibility.<sup>[8]</sup> Whereas, as mentioned earlier, ultra-narrow band laser camouflage materials cannot cope with laser detectors with tunable broadband wavelength. Shaping a structure to redirect the incoming waves to non-threatening angles could also reduce echo signals. Nevertheless, it is still non-ideal due to the complexity of design and incompatibility with aero- and hydro-dynamics.<sup>[11,41]</sup> Here, we design an all-metallic metasurface containing two subgroups (**Figure 1b**) to realize dual-band lasers camouflage by shaping their electromagnetic wavefronts.



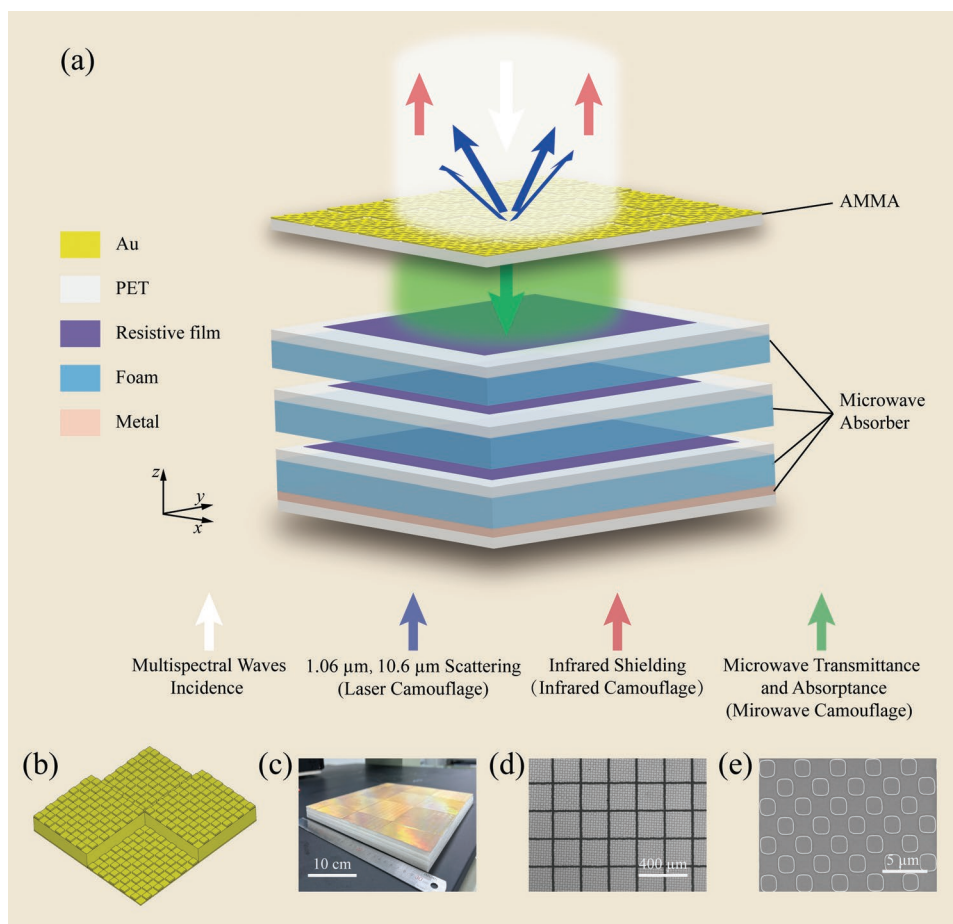


**Figure 1.** Schematic of the proposed MHM for laser-infrared-microwave compatible camouflage and images of the fabricated sample. a) Concept illustration of the camouflage principles in different bands. When the multispectral electromagnetic waves incident on the device, the infrared light will be reflected, the light in a dual-band involving the wavelengths of 1.06  $\mu\text{m}$  and 10.6  $\mu\text{m}$  will be guided to non-specular angles, and the microwave will transmit through the AMMA and then be absorbed. Therefore, the compatible camouflage of dual-band lasers, infrared and microwave can be realized. b) Schematic of the all-metallic metasurface. c) The photograph of the fabricated MHM sample. d, e) Optical microscope (OM) image and scanning electron microscopy (SEM) image of the AMMA, respectively.

In each subgroup, there are two unit cells, as depicted in insets of **Figure 2a,d**, which are arranged in a chessboard-like configuration. Based on the transmission phase, a  $180^\circ$  phase abrupt change between adjacent unit cells is constructed. As a result, destructive interference of the reflected waves will be produced, which could lead to a null in the specular direction and result in a reduction of echo signals. For the subgroup I (working in the band containing 1.06  $\mu\text{m}$ ), unit cell I is a gold plate with a thickness of 0.2  $\mu\text{m}$ , and a period of  $\Lambda_1 = 2 \mu\text{m}$ ; unit cell II consists of a gold cube placed on a gold plate with the same thickness and period as unit cell I. The geometry parameters of the gold cube are  $d_1 = 1.8 \mu\text{m}$  and  $h_1 = 0.27 \mu\text{m}$ . For the subgroup II (working in the band containing 10.6  $\mu\text{m}$ ), the corresponding geometric parameters are  $\Lambda_2 = 20 \mu\text{m}$ ,  $d_2 = 20 \mu\text{m}$  and  $h_2 = 2.8 \mu\text{m}$ . **Figure 2a,d** shows the wavelength dependence of the reflection amplitude. For each subgroup, the reflection phases of its two unit cells, as well as relative phase difference ( $\Delta\Phi = |\Phi_2 - \Phi_1|$ , where  $\Phi_1$  and  $\Phi_2$  are the reflection phases of the unit cell I and unit cell II, respectively) between them are presented in **Figure 2b,e**, respectively. One

can see that the reflection amplitudes are higher than 90%, and  $\Delta\Phi$  is approximately equal to  $\pi$  in the dual-band, which implies destructive interference between the reflected waves from these unit cells is produced. The reflected electric field distributions at the wavelengths of 1.06 and 10.6  $\mu\text{m}$  are given in **Figure S2a,d** (Supporting Information), respectively; typical patterns of destructive interference can be observed. Further, simulations for each subgroup were conducted to calculate the amplitude of zero-order light (corresponding to the specular reflectance). The results are displayed in **Figure 2c,f**, from which we can see that the reflectance in both bands are  $<0.1$ . For a given chessboard-like configuration, the reflected field direction ( $\theta, \varphi$ ) of incident light with a wavelength of  $\lambda$  and incidence angle of  $(\theta_0, \varphi_0)$  can be predicted theoretically by the following formulas:<sup>[41,42]</sup>

$$\tan \varphi = \frac{\sin \theta_0 \sin \varphi_0 \pm (2n + 1) \frac{\lambda}{2d_y}}{\sin \theta_0 \cos \varphi_0 \pm (2m + 1) \frac{\lambda}{2d_x}} \quad (1)$$

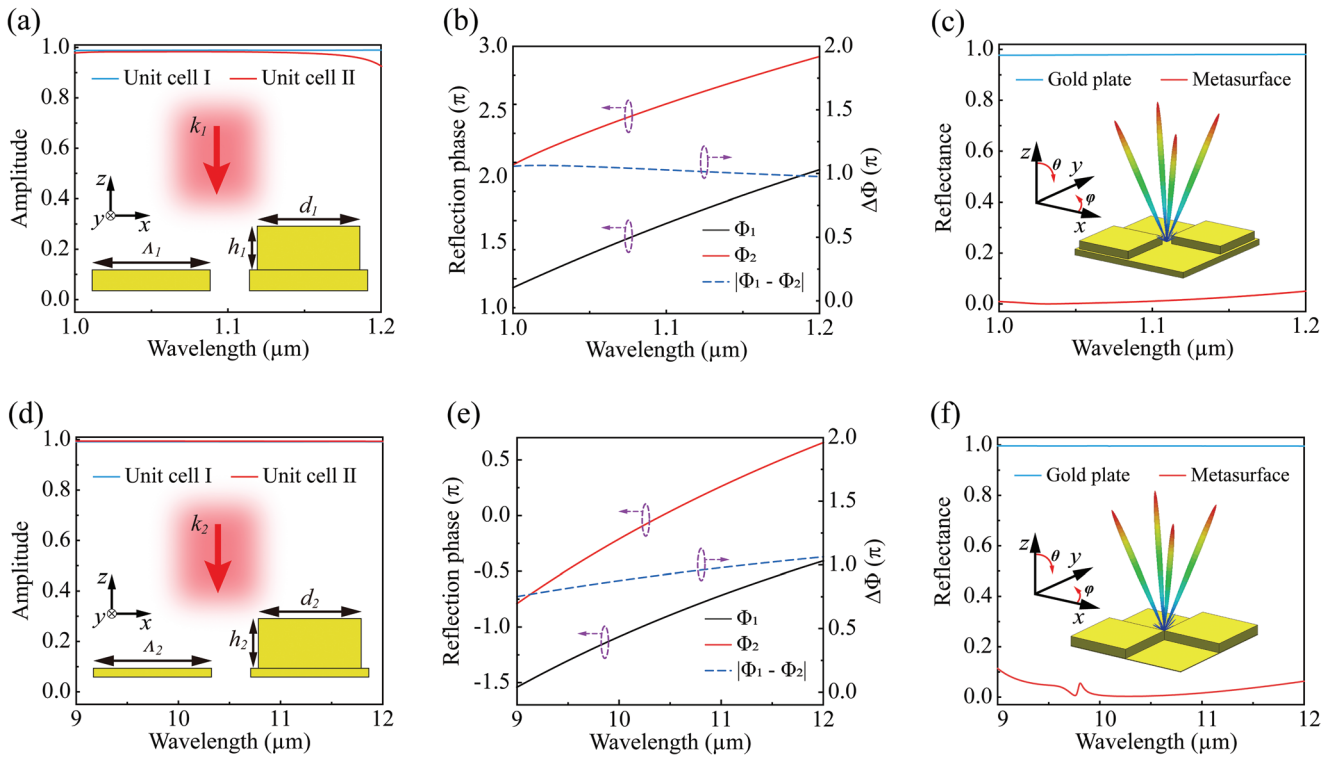


**Figure 2.** Simulated results of the a–c) subgroup I and d–f) subgroup II. a,d) Reflection amplitudes of the unit cells. Inserts show the schematic view of each unit cell. b,e) Reflection phases of the unit cells, as well as the relative phase difference between them. c,f) Specular (zero-order) reflection spectra of the two subgroups and the gold plates under normal incidence in 1–1.2 and 9–12  $\mu\text{m}$ . Inserts of (c,f) show the 3D far-field scattering patterns of the subgroups at 1.06 and 10.6  $\mu\text{m}$ , respectively.

$$\sin \theta = \frac{\sin \theta_0 \sin \varphi_0 \pm (2n+1) \frac{\lambda}{2d_y}}{\sin \varphi} \quad (2)$$

$$= \frac{\sin \theta_0 \cos \varphi_0 \pm (2m+1) \frac{\lambda}{2d_x}}{\cos \varphi}$$

where  $d_x$  and  $d_y$  are the dimensions of the unit cell along the  $x$ - and  $y$ -axis,  $n + m + 1$  defines the order of the grating lobes. In our case (i.e.,  $d_x = d_y$ ;  $n = m = 0$ ), at the normal incidence, the reflected field direction ( $\theta$ ,  $\varphi$ ) can be calculated by the following formulas:

$$\tan \varphi = \pm \frac{d_x}{d_y} = \pm 1 \quad (3)$$

$$\sin \theta = \pm \frac{\lambda}{\sqrt{2}d_y} = \pm \frac{\lambda}{\sqrt{2}d_x} \quad (4)$$

In our designs, scattering field directions of 1.06  $\mu\text{m}$  (i.e.,  $d_x = d_y = 2 \mu\text{m}$ ) and 10.6  $\mu\text{m}$  (i.e.,  $d_x = d_y = 20 \mu\text{m}$ ) are consistent, which can be calculated according to Equations (3) and (4). The azimuth is equal to  $\varphi = \pm 45^\circ$ , which indicates that the reflected energy is mainly concentrated on the  $45^\circ$  and  $-45^\circ$  planes. The elevation angles are calculated to be  $\theta = \pm 22^\circ$ . The simulated 3D far-field scattering patterns at 1.06 and 10.6  $\mu\text{m}$  are given in inserts of Figure 2c,f, respectively, together with the scattering patterns at  $\varphi = 45^\circ$  (or  $-45^\circ$ ) plane in Figure S2b,e (Supporting Information). It is evident that the reflected energy is spilt into four diagonal directions in the  $45^\circ$  and  $-45^\circ$  plane and the

reflection elevation angles are  $\theta = \pm 22^\circ$ , which is in great agreement with the theoretical calculations. In comparison, the specular ( $\theta = 0^\circ$ ) reflectance is close to zero. In addition, full-wave simulations were performed to confirm the performance of the all-metallic metasurface which combines the abovementioned two subgroups. The simulated 3D far-field scattering patterns at 1.06 and 10.6  $\mu\text{m}$  are illustrated in Figure S2c,f (Supporting Information), respectively, showing that, for both wavelengths, this metasurface could considerably reflect the energy away from the normal direction. These simulated results above prove that the all-metallic metasurface can achieve remarkable echo signals reduction in a dual-band.

According to the Stefan–Boltzmann's law  $Q = \varepsilon \sigma T^4$ , the infrared signature from an object is related to the surface emissivity  $\varepsilon$  and surface temperature  $T$ . Our strategy to achieve infrared camouflage is to adjust the surface emissivity  $\varepsilon$  of the device. In general, low surface infrared emissivity could disguise the targets from thermal infrared detectors. As we mentioned previously, periodically arranged all-metallic metasurfaces form the AMMA as shown in Figure S4a (Supporting Information), where the patch width  $d$  and period  $p$  are 200 and 220  $\mu\text{m}$ , respectively. Meanwhile, full-wave simulations show that low infrared emissivity of the all-metallic metasurface can be kept in 3–5  $\mu\text{m}$  and 8–14  $\mu\text{m}$  (Figure S5, Supporting Information). Combining with a high filling ratio (82.6%) of the all-metallic metasurface, the AMMA can effectively reduce the surface infrared emissivity of the MHM. Specifically, the average surface infrared emissivity in 3–5  $\mu\text{m}$  and 8–14  $\mu\text{m}$  can be

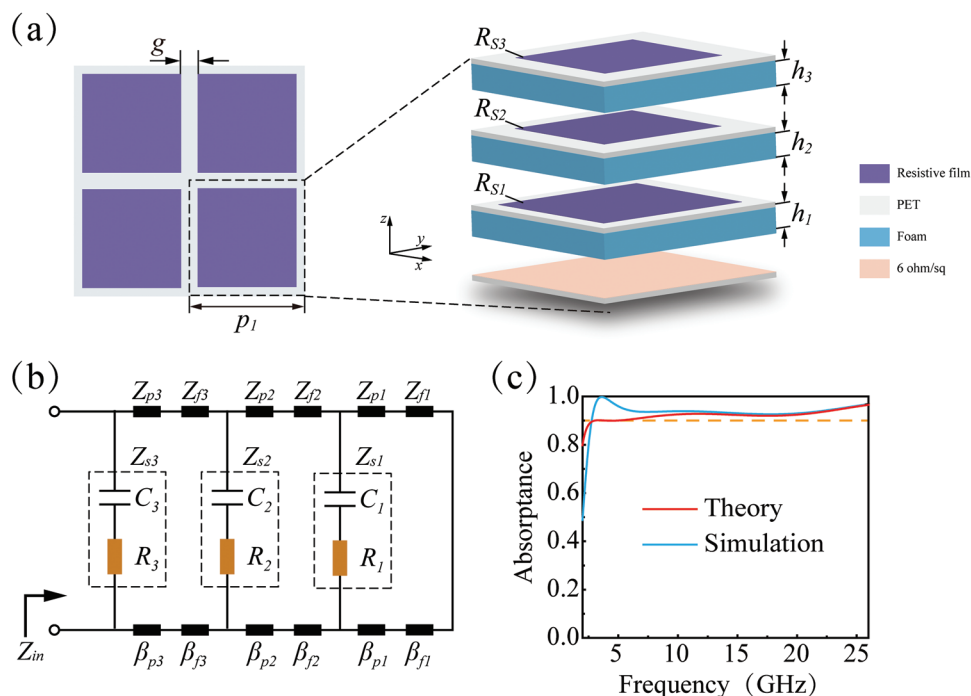


**Figure 3.** Design and simulation of the microwave absorber. a) Schematic of the microwave absorber. The optimized parameters are  $p_1 = 10$  mm,  $g_1 = 0.2$  mm,  $g_2 = g_3 = 1.5$  mm.  $h_1 = h_2 = 4$  mm,  $h_3 = 3$  mm,  $R_{s1} = 150 \Omega \text{ sq}^{-1}$ ,  $R_{s2} = R_{s3} = 300 \Omega \text{ sq}^{-1}$ . b) The equivalent circuit of the proposed absorber. c) The absorbance spectra of the absorber in 2–26 GHz obtained by equivalent circuit model and numerical simulation.

calculated approximately to be 0.181 and 0.166, respectively by an empirical formula (see Section S2 in the Supporting Information for details).

In order to achieve invisibility against microwave detection, broadband high absorption is vital. Here, an ultra-broadband microwave absorber consisting of trilayered square patch metasurfaces on 125- $\mu\text{m}$ -thick PET, intermediate foam spacers with distinctive thicknesses and a reflective ground plane providing zero transmittance is designed to realize microwave camouflage (the schematic is shown in Figure 3a). Continuous indium tin oxide (ITO) film with the resistance of  $6 \Omega \text{ sq}^{-1}$  is adopted as the reflective plane. The equivalent circuit of our microwave absorber is presented in Figure 3b, where the square patch metasurface can be equivalent to the series connection of a resistor and a capacitor.<sup>[43,44]</sup> For  $i$ th ( $i = 1, 2$ , or  $3$ ) square patch metasurface with gap  $g_i$ , period  $p$ , and resistance  $R_{si}$ , the intensity of the electric fields between the gaps would follow a catenary curve, and the effective impedance  $Z_{si}$  can also be expressed with the catenary functions.<sup>[18]</sup> The characteristic impedances  $Z_{fi}$  and  $Z_{pi}$  of dielectric layers are defined by their dielectric constants. The dielectric constants of foam and PET are  $\epsilon_f = 1.07(1-j0.0026)$  and  $\epsilon_p = 3(1-j0.06)$ , respectively.  $\beta$  indicates the propagation constant in the dielectric. By utilizing the transmission line theory (see Section S3 in the Supporting Information for details),<sup>[18,45,46]</sup> the reflectance coefficient of the absorber which depends on the input impedance  $Z_{in}$  can be obtained as

$$r(p, g, R_s, \lambda, h) = \left| \frac{Z_{in} - Z_0}{Z_{in} + Z_0} \right| \quad (5)$$

where  $Z_0 = 377 \Omega$  is the free-space impedance. Thereupon, the absorbance can be easily calculated as  $A = 1 - r^2$  since the bottom reflective plane provides a zero transmittance ( $t = 0$ ). Based on this model, the absorption performance was optimized, and the related parameters are given in the caption of Figure 3. Figure 3c illustrates the theoretically calculated and the numerically simulated absorption spectra, which are in general agreement with each other and both show that the absorbance remains higher than 90% in 2.7–26 GHz. In order to further figure out the broadband absorption physical mechanism, the surface current, the magnetic field, and the surface power loss density distributions at three frequencies of 3.4, 12, and 24 GHz are provided (see Section S3 in the Supporting Information for details).

In the following, we consider the microwave absorption capacity after integrating the microwave absorber and the AMMA. Because there are more than 10 million metallic cubes located on the AMMA in a unit cell of the microwave absorber, numerical simulations cannot be conducted owing to the computer's computing power limitation if the AMMA is used. Considering the height of the metallic cubes in the AMMA is in the micrometer range, for the microwave whose wavelength is on the order of centimeter, the AMMA can be equivalent to a metallic patch array without cubes, which acts as a capacitive frequency selective surface<sup>[10]</sup> and is transparent to the incident microwave in a certain band (Figure S8, Supporting Information). Therefore, it is reasonable to use the metallic patch array without cubes in the simulation to confirm the microwave camouflage performance of the MHM. The corresponding simulated result shows that high absorbance above 90% between 2.7 and 26 GHz can still be kept (Figure S9, Supporting Information).

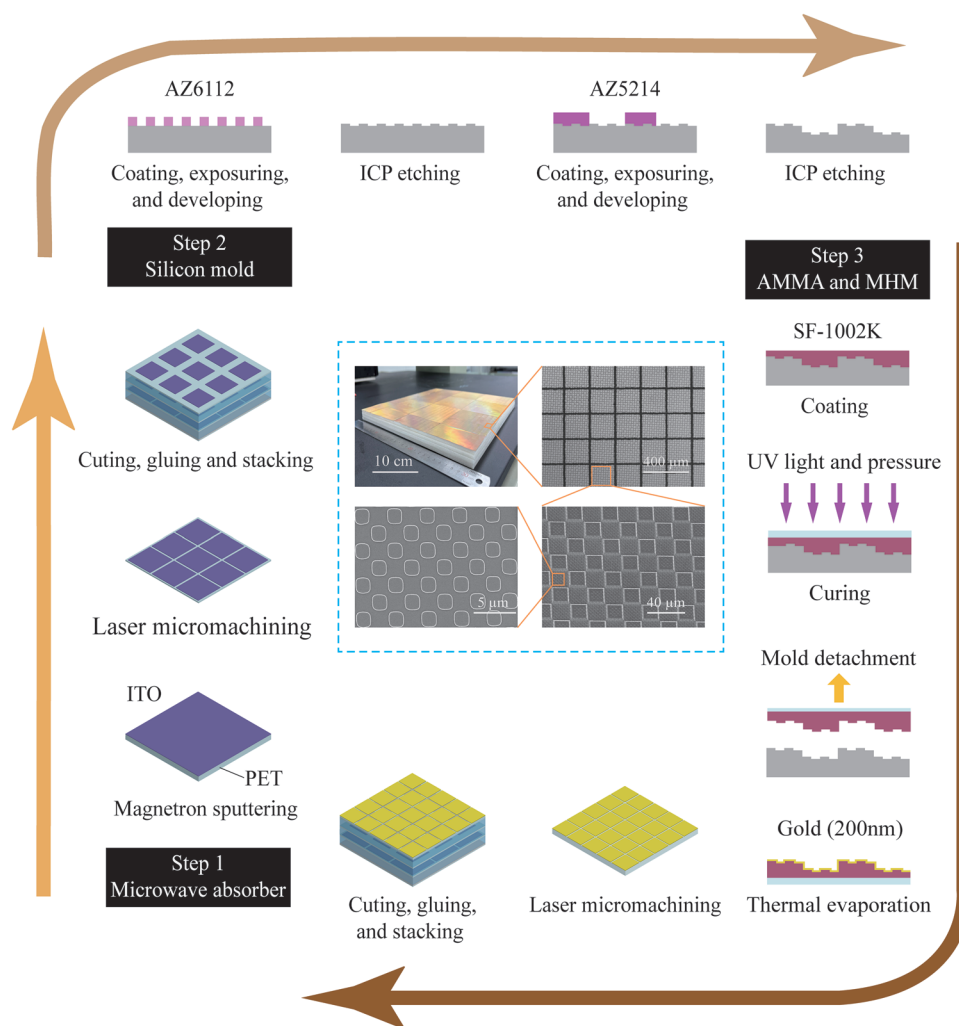


**Figure 4.** Schematic diagrams for the fabrication process used for the microwave absorber, the silicon mold, the AMMA and the MHM. The insets show the photograph, OM and SEM images of the prepared MHM sample.

### 3. Fabrication and Characterization

To further investigate the multispectral compatible camouflage performance experimentally, a MHM sample with an area of  $30 \times 30 \text{ cm}^2$  and a minimum linewidth of  $1.8 \mu\text{m}$  was fabricated. **Figure 4** illustrates the detailed fabrication process. The first step is the fabrication of the microwave absorber. Different thickness of ITO layers was grown by magnetron sputtering technology to obtain desired sheet resistance, and the patterns were prepared using laser micromachining. The second step is the preparation of a 6-inch silicon mold with a pattern complementary to the all-metallic metasurface (see the Experimental Section for details). The third step involves fabricating the AMMA and the MHM. Conventional ultraviolet (UV) NIL was used to fabricate the all-metallic metasurface (see the Experimental Section for details). The key advantages of NIL are its low cost, high throughput, and high resolution. Because UV NIL hardens the resin employing ultraviolet light instead of heat source, no heating and cooling process is required, leading to a more productive fabrication. It should be noted that limited by our processing equipment, the

most basic UV NIL method was used here to prove the concept we put forward. In fact, many other advanced NIL methods can be used for more continuous and high-yield fabrication.<sup>[47–49]</sup> Then, the micrometer-scale slits in the AMMA were manufactured by laser micromachining. Finally, after cutting, gluing and stacking, the MHM sample with laser-infrared-microwave compatible camouflage function was obtained.

After obtaining the sample, the performance of multispectral compatible camouflage was characterized. We first measured the reflectances of the AMMA by a spectrophotometer for the near-infrared regime and by a Fourier-transform infrared (FTIR) spectrometer for the far-infrared regime. The measured reflectances in  $0.9\text{--}1.2 \mu\text{m}$  and  $9\text{--}12 \mu\text{m}$  are presented in **Figure 5a,b**, which are  $<0.15$  for both TE and TM polarizations. The slight inconsistency between measured results and simulated results can be attributed to the fabrication imperfections and measurement errors. In comparison, the unpatterned gold plate has much higher reflectance. Moreover, our sample shows excellent wide-angle responses in the dual-band as depicted in Figures S10–S11 (Supporting Information). We then measured the microwave



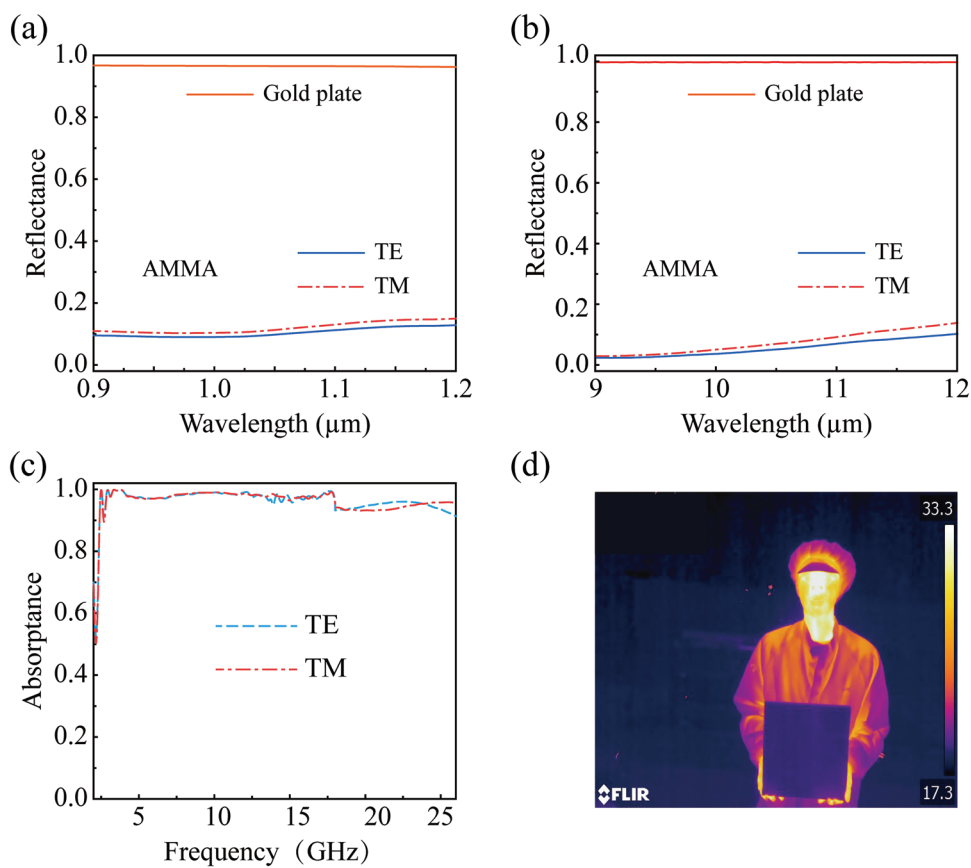


**Figure 5.** Measured reflectance spectra of the AMMA under TE and TM polarized incidences in a) 0.9–1.2  $\mu\text{m}$  and b) 9–12  $\mu\text{m}$ . c) Measured absorbance spectra of the MHM under TE and TM polarized incidences in 2–26 GHz. d) Thermal infrared image of the fabricated sample held by the researcher in the laboratory at room temperature.

absorption property, and the results are displayed in Figure 5c. The results obtained by the experiment agree well with those by the theoretical and simulated results, showing that this absorber could considerably attenuate the light energy by over 90% in a wide frequency band of 2.7–26 GHz. The absorption properties of the fabricated absorber under different incidence angles were also tested (Figure S12, Supporting Information). As the incidence angle increases, the absorption bandwidth begins to decrease, while the microwave absorber still keeps high absorbance above 90% between 4.9 and 26 GHz even under 45° oblique incidence. Finally, the infrared camouflage performance of the MHM sample was characterized by commercial infrared imagers. As shown in Figure 5d, the thermal radiation from the human body is totally shielded by the sample whose radiation temperature is comparable to the ambient temperature. In addition, in order to further illustrate that the as-prepared AMMA has low thermal infrared emissivity, the comparison of thermal infrared images between an AMMA sample, an all-metallic metasurface sample, a gold plate, and a PET film at a heating plate with a temperature of 65 °C is given in Figure S13 (Supporting Information). According to the Stefan–Boltzmann’s law, when the surface temperature is the same, samples with lower radiation temperatures have lower emissivity. The measured radiation temperature of the AMMA is little higher than that of the all-metallic metasurface and gold plate since the periodical

slits existing in it, however, is still much lower than that of the PET film. Therefore, the overall measured results confirm the compatible camouflage performance of dual-band lasers, infrared and microwave.

#### 4. Conclusion

In summary, this article demonstrates, for the first time, the metasurface-based structure to realize dual-band lasers, infrared and microwave compatible camouflage. The presented multi-scale-hierarchical metasurfaces (MHM) can manipulate electromagnetic waves in the wide spectrum range of wavelength from micrometers to centimeters. At the same time, large-area low-cost fabrication of this multiscale structure (i.e., feature sizes spanning four orders of magnitude) is achieved based on nano-imprint lithography. Moreover, based on this method, utilizing metasurfaces with more steps to achieve compatibility with more bands is foreseeable. The excellent compatible camouflage performance is verified in the consistent simulated and experiment results, showing low reflectance (<0.2) in 0.9–1.2  $\mu\text{m}$  and 9–12  $\mu\text{m}$ , low infrared emissivity (<0.2), and high absorbance of over 90% in 2.7–26 GHz. Wide-angle and polarization-independent characteristics are also demonstrated. These results not only break through the limitation of conventional compatible



camouflage materials in performance, but also open an exciting route to achieve large-area low-cost fabrication of multispectral camouflage materials. In addition, our designed structure holds potential for flexible and transparent multispectral camouflage (see Section S7 in the Supporting Information for details). Therefore, this work may promote the engineering applications of metasurfaces in the field of multispectral camouflage. Moreover, the remarkable capability as exhibited by this approach to modulate multispectral electromagnetic waves makes it have potential applications in other multispectral devices.

## 5. Experimental Section

**Simulation:** Numerical simulations were conducted using commercial software CST Microwave Studio. Simulations for the two subgroups and infrared absorption of the all-metallic metasurface, as well as the microwave transmittance of the AMMA and the microwave absorption were performed in frequency domain solver, unit cell boundary was applied in both  $x$ - and  $y$ -directions and the open boundary was adopted in the  $z$ -direction. Simulations for the 3D far-field scattering patterns of the all-metallic metasurface were conducted in a time domain solver with periodic boundary in both  $x$ - and  $y$ -axis and open boundary in the  $z$ -axis, a plane wave with  $x$  polarization propagating along the negative  $z$ -axis was used as the excitation. The permittivity of gold is from Ref. [50].

**Fabrication:** First, a 6-inch hard mold with a pattern complementary to the all-metallic metasurface was obtained by two-step photolithography. The photolithography started with coating a silicon wafer with a photoresist layer. The first pattern (subgroup I) on the mask was transferred to the photoresist through lithography exposure. After developing, an inductive coupled plasmonic (ICP) etching was utilized to transfer photoresist patterns into the silicon wafer to form the desired structure. In a similar way, the second pattern (subgroup II) was subsequently fabricated on the silicon wafer, resulting in the desired silicon mold (Figure S14b, Supporting Information). Second, a typical UV NIL process was performed to pattern photopolymer resin. Specifically, after the liquid resin was coated on the silicon mold and covered with UV-transparent PET substrate, the resin was continuously imprinted by a roller and cured with exposure to UV light. Then, the PET substrate with rigid and patterned resin was separated from the mold (Figure S14c, Supporting Information). Finally, a 200 nm Au layer was deposited onto the patterned resin via thermal evaporation, and an all-metallic metasurface sample was obtained (Figure S13d, Supporting Information).

**Measurement:** Since the  $30 \times 30$  cm<sup>2</sup> sample is too large for the measuring instruments, a  $2 \times 2$  cm<sup>2</sup> piece was randomly cut from the as-prepared AMMA sample to investigate the dual-band lasers camouflage performance. The reflectances in 0.9–1.2  $\mu$ m and 9–12  $\mu$ m were measured using the spectrophotometer (Lambda 1050, PerkinElmer) and the Fourier transform infrared (FTIR) spectrometer (Vertex 80, Bruker), respectively. The minimal test angles of the two instruments can only be adjusted to 8 and 15°, respectively. A same size gold plate without subwavelength structures was measured for comparison. The performance of the microwave absorber was tested by an arch measurement system with a vector network analyzer (Rohde & Schwarz ZVA40) in the anechoic chamber. Several pairs of high gain horn antennas working in different bands were employed. The thermal infrared images in Figure 5d and Figure S13b (Supporting Information) were taken with a long-wavelength infrared camera (FLIR T650sc) operating at 7.5–14  $\mu$ m. The thermal infrared image in Figure S13a (Supporting Information) was taken with a mid-wavelength infrared camera (IR-Core MW615) operating at 3–5  $\mu$ m. Informed signed consent was obtained from the volunteer for the thermal infrared image in Figure 5d.

## Supporting Information

Supporting Information is available from the Wiley Online Library or from the author.

## Acknowledgements

This work was supported by the National Natural Science Foundation of China (U20A20217, 61975210, and 62175242), the China Postdoctoral Science Foundation (2020M680153), and the National Key Research and Development Program of China (SQ2021YFA1400121).

## Conflict of Interest

The authors declare no conflict of interest.

## Data Availability Statement

The data that support the findings of this study are available from the corresponding author upon reasonable request.

## Keywords

compatible camouflage, infrared, lasers, microwave, multiscale structures, multispectral manipulation

Received: May 16, 2022

Revised: June 9, 2022

Published online: July 5, 2022

- [1] M. Stevens, I. C. Cuthill, *Proc. R. Soc. B Biol. Sci.* **2006**, 273, 2141.
- [2] I. C. Cuthill, M. Stevens, J. Sheppard, T. Maddocks, C. A. Párraga, T. S. Troscianko, *Nature* **2005**, 434, 72.
- [3] J. Skelhorn, H. M. Rowland, M. P. Speed, G. D. Ruxton, *Science* **2010**, 327, 51.
- [4] L. A. Nilsson, *Nature* **1983**, 305, 799.
- [5] M. Stevens, W. T. L. Searle, J. E. Seymour, K. L. Marshall, G. D. Ruxton, *BMC Biol.* **2011**, 9, 81.
- [6] M. Stevens, S. Merilaita, *Philos. Trans. R. Soc. B Biol. Sci.* **2009**, 364, 423.
- [7] T. Yang, X. Bai, D. Gao, L. Wu, B. Li, J. T. L. Thong, C. Qiu, *Adv. Mater.* **2015**, 27, 7752.
- [8] H. Zhu, Q. Li, C. Tao, Y. Hong, Z. Xu, W. Shen, S. Kaur, P. Ghosh, M. Qiu, *Nat. Commun.* **2021**, 12, 1805.
- [9] T. Wang, J. He, J. Zhou, X. Ding, J. Zhao, S. Wu, Y. Guo, *Microporous Mesoporous Mater.* **2010**, 134, 58.
- [10] H. Tian, H.-T. Liu, H.-F. Cheng, *Chin. Phys. B* **2014**, 23, 025201.
- [11] X. Xie, X. Li, M. Pu, X. Ma, K. Liu, Y. Guo, X. Luo, *Adv. Funct. Mater.* **2018**, 28, 1706673.
- [12] X. Feng, X. Xie, M. Pu, X. Ma, Y. Guo, X. Li, X. Luo, *Opt. Express* **2020**, 28, 9445.
- [13] E. F. Knott, J. F. Schaeffer, M. T. Tully, *Radar Cross Section*, 2nd ed., SciTech, Raleigh, NC, USA **2004**.
- [14] H. Ahmad, A. Tariq, A. Shehzad, M. S. Faheem, M. Shafiq, I. A. Rashid, A. Afzal, A. Munir, M. T. Riaz, H. T. Haider, A. Afzal, M. B. Qadir, Z. Khaliq, *Polym. Compos.* **2019**, 40, 4457.
- [15] M. Pan, Y. Huang, Q. Li, H. Luo, H. Zhu, S. Kaur, M. Qiu, *Nano Energy* **2020**, 69, 104449.
- [16] J.-J. Greffet, M. Nieto-Vesperinas, *J. Opt. Soc. Am. A* **1998**, 15, 2735.
- [17] M. Pu, X. Li, X. Ma, Y. Wang, Z. Zhao, C. Wang, C. Hu, P. Gao, C. Huang, H. Ren, X. Li, F. Qin, J. Yang, M. Gu, M. Hong, X. Luo, *Sci. Adv.* **2015**, 1, e1500396.
- [18] Y. Huang, J. Luo, M. Pu, Y. Guo, Z. Zhao, X. Ma, X. Li, X. Luo, *Adv. Sci.* **2019**, 6, 1801691.

- [19] X. Luo, M. Pu, Y. Guo, X. Li, F. Zhang, X. Ma, *Adv. Opt. Mater.* **2020**, 8, 2001194.
- [20] F. Zhang, M. Pu, X. Li, X. Ma, Y. Guo, P. Gao, H. Yu, M. Gu, X. Luo, *Adv. Mater.* **2021**, 33, 2008157.
- [21] J. Engelberg, C. Zhou, N. Mazurski, J. Bar-David, A. Kristensen, U. Levy, *Nanophotonics* **2020**, 9, 361.
- [22] Z. Deng, M. Jin, X. Ye, S. Wang, T. Shi, J. Deng, N. Mao, Y. Cao, B. Guan, A. Alù, G. Li, X. Li, *Adv. Funct. Mater.* **2020**, 30, 1910610.
- [23] Z. Li, C. Chen, Z. Guan, J. Tao, S. Chang, Q. Dai, Y. Xiao, Y. Cui, Y. Wang, S. Yu, G. Zheng, S. Zhang, *Laser Photonics Rev.* **2020**, 14, 2000032.
- [24] H. Gao, X. Fan, W. Xiong, M. Hong, *Opto-Electron. Adv.* **2021**, 4, 210030.
- [25] L. Jin, Y.-W. Huang, Z. Jin, R. C. Devlin, Z. Dong, S. Mei, M. Jiang, W. T. Chen, Z. Wei, H. Liu, J. Teng, A. Danner, X. Li, S. Xiao, S. Zhang, C. Yu, J. K. W. Yang, F. Capasso, C.-W. Qiu, *Nat. Commun.* **2019**, 10, 4789.
- [26] F. Zhang, M. Pu, X. Li, P. Gao, X. Ma, J. Luo, H. Yu, X. Luo, *Adv. Funct. Mater.* **2017**, 27, 1704295.
- [27] J. Li, P. Yu, S. Zhang, N. Liu, *Nat. Commun.* **2020**, 11, 3574.
- [28] T. Cao, M. Lian, X. Chen, L. Mao, K. Liu, J. Jia, Y. Su, H. Ren, S. Zhang, Y. Xu, J. Chen, Z. Tian, D. Guo, *Opto-Electron. Sci.* **2021**, 1, 210010.
- [29] X. Xie, M. Pu, J. Jin, M. Xu, Y. Guo, X. Li, P. Gao, X. Ma, X. Luo, *Phys. Rev. Lett.* **2021**, 126, 183902.
- [30] X. Luo, M. Pu, F. Zhang, M. Xu, Y. Guo, X. Li, X. Ma, *J. Appl. Phys.* **2022**, 131, 181101.
- [31] J. Liu, M. Shi, Z. Chen, S. Wang, Z. Wang, S. Zhu, *Opto-Electron. Adv.* **2021**, 4, 200092.
- [32] S. Chen, W. Liu, Z. Li, H. Cheng, J. Tian, *Adv. Mater.* **2020**, 32, 1805912.
- [33] Y. Zhu, X. Chen, W. Yuan, Z. Chu, K. Wong, D. Lei, Y. Yu, *Opto-Electron. Adv.* **2021**, 4, 210013.
- [34] X. Ni, Z. J. Wong, M. Mrejen, Y. Wang, X. Zhang, *Science* **2015**, 349, 1310.
- [35] M. Pu, Z. Zhao, Y. Wang, X. Li, X. Ma, C. Hu, C. Wang, C. Huang, X. Luo, *Sci. Rep.* **2015**, 5, 9822.
- [36] T. Kim, J. Bae, N. Lee, H. H. Cho, *Adv. Funct. Mater.* **2019**, 29, 1807319.
- [37] C. Zhang, X. Wu, C. Huang, J. Peng, C. Ji, J. Yang, Y. Huang, Y. Guo, X. Luo, *Adv. Mater. Technol.* **2019**, 4, 1900063.
- [38] C. Zhang, C. Huang, M. Pu, J. Song, Z. Zhao, X. Wu, X. Luo, *Sci. Rep.* **2017**, 7, 5652.
- [39] X. Xie, M. Pu, Y. Huang, X. Ma, X. Li, Y. Guo, X. Luo, *Adv. Mater. Technol.* **2019**, 4, 1800612.
- [40] J.-K. Zhang, J.-M. Shi, D.-P. Zhao, Q.-C. Wang, C.-M. Wang, *Infrared Phys. Technol.* **2017**, 85, 62.
- [41] W. Chen, C. A. Balanis, C. R. Birtcher, *IEEE Trans. Antennas Propag.* **2015**, 63, 2636.
- [42] J. C. Iriarte Galarregui, A. Tellechea Pereda, J. L. M. de Falcon, I. Ederra, R. Gonzalo, P. de Maagt, *IEEE Trans. Antennas Propag.* **2013**, 61, 6136.
- [43] C. S. R. Kaipa, A. B. Yakovlev, F. Medina, F. Mesa, *J. Appl. Phys.* **2012**, 112, 033101.
- [44] O. Luukkonen, C. Simovski, G. Granet, G. Goussetis, D. Lioubtchenko, A. V. Räisänen, S. Tretyakov, *IEEE Trans. Antennas Propag.* **2008**, 56, 1624.
- [45] X. Luo, *Sci. China Phys. Mech. Astron.* **2015**, 58, 594201.
- [46] F. Costa, A. Monorchio, G. Manara, *IEEE Antennas Propag. Mag.* **2012**, 54, 35.
- [47] S. H. Ahn, L. J. Guo, *ACS Nano* **2009**, 3, 2304.
- [48] J. G. Ok, H. Seok Youn, M. Kyu Kwak, K.-T. Lee, Y. Jae Shin, L. Jay Guo, A. Greenwald, Y. Liu, *Appl. Phys. Lett.* **2012**, 101, 223102.
- [49] N. Atthi, M. Dielen, W. Sripumkhai, P. Pattamang, R. Meananetra, P. Saengdee, O. Thongsook, N. Ranron, K. Pankong, W. Uahchinkul, J. Supadech, N. Klunngien, W. Jeamsaksiri, P. Veldhuizen, J. M. ter Meulen, *Nanomaterials* **2021**, 11, 339.
- [50] E. D. Palik, *Handbook of Optical Constants of Solids*, Academic Press, **1998**.